Physics of Plasmas ARTICLE scitation.org/journal/php

Quantitative analysis of multipactor threshold sensitivity to secondary emission yield of microwave devices

Cite as: Phys. Plasmas **30**, 033104 (2023); doi: 10.1063/5.0138875
Submitted: 15 December 2022 · Accepted: 10 February 2023 ·
Published Online: 7 March 2023

View Online

Export Citation

CrossMark

Shu Lin,[1,2,3] Hao Qu,[1,2] Ning Xia,[1,2] Patrick Wong,[3] Peng Zhang,[3] John Verboncoeur,[3] Meng Cao,[1,2] Yonggui Zhai,[1,2] Yongdong Li,[1,2] and Hongguang Wang[1,2,a)]

AFFILIATIONS

[1]Key Laboratory for Physical Electronics and Devices of the Ministry of Education, Xi'an Jiaotong University, Xi'an 710049, China
[2]School of Electronic Science and Engineering, Xi'an Jiaotong University, Xi'an 710049, China
[3]Department of Electrical and Computer Engineering, Michigan State University, East Lansing, Michigan 48824, USA

[a)]Author to whom correspondence should be addressed: wanghg@mail.xjtu.edu.cn

ABSTRACT

Multipactor occurrence essentially depends on the secondary emission property of the surface material, which is, thus, the requisite input for multipactor threshold prediction using the numerical and theoretical approaches. However, secondary emission yield (SEY) deviation in experimental measurements inevitably leads to uncertainty error in multipactor threshold prediction. Therefore, this paper presents a thorough quantitative analysis of multipactor threshold sensitivity to SEY including the effect of the device geometry, the multipactor mode, and the material type. Based on the statistical modeling, multipactor threshold voltages with respect to the SEY variation in critical SEY regions are calculated for both the parallel plates and coaxial lines with different multipactor orders and typical materials. Furthermore, the distribution of electron impact energy is also obtained to elucidate the underlying mechanism for the relevant sensitivity discrepancy. The result reveals that multipactor threshold is generally most sensitive to the energy region below the first crossover energy (E_1), and this is changed to higher energies below the corresponding energy to the SEY maximum (E_m) with a change in the device geometry, multipactor mode, or coating material. It is also found that the magnitude relation of the threshold sensitivity between different regions is radically determined with the distribution of electron impact energy, and the SEY variation close to E_m merely affects the threshold result with a high multipactor order. This research provides useful reference for properly determining the threshold margin from the measurement error of SEY, thus promoting the performance optimization with multipactor prevention in the practical application of microwave devices.

Published under an exclusive license by AIP Publishing. https://doi.org/10.1063/5.0138875

I. INTRODUCTION

Microwave devices operating with a high-power level and near-vacuum condition are prone to suffer potential risk of multipactor breakdown,[1] which is an electromagnetic phenomenon substantially driven by secondary electron avalanche and ubiquitously seen in microwave tubes, RF antennas and windows, particle accelerators, and space communication payloads.[2–4] Recent development of space communication techniques requires microwave systems to achieve a higher power capacity and further device miniaturization, which accordingly exacerbates the risk of multipactor. Because of the catastrophic hazard of multipactor,[5] it must be ensured that no multipactor occurs during practical device operation for engineering applications.

For the sake of operational durability and reliability, the satellite-borne microwave components in the qualification stage conventionally require experimental test to determine whether multipactor occurs or not, which can be fulfilled with the third harmonic detection or phase nulling methods.[6,7] However, regarding expensive experimental cost, the theoretical[8–10] and numerical[11,12] approaches for predicting multipactor threshold are more commonly employed for the optimum design of microwave devices, which, thus, are practically required to operate below the multipactor threshold voltage with additional margin applied in view of inevitable error in multipactor threshold prediction. Yet, this also makes the practical performance of device operation strongly constrained by the threshold prediction accuracy. In view of the inherent dependence of multipactor occurrence on the secondary emission property, the proper calculation of multipactor threshold needs to take the whole distribution of secondary emission yield (SEY) measured from the experimental samples into consideration.

As a matter of fact, the SEY value at the specified impact energy is commonly determined with the result average of multiple SEY measurements at different positions on the experimental samples.[13] Thus, the result fluctuation of SEY generally arises from the measurement error of SEY and the spatial SEY discrepancy on the experimental sample, which accordingly leads to inaccuracy in the calculation result of multipactor threshold. Furthermore, it is still difficult to perform accurate SEY measurement for the energy region within tens of eVs due to the limitation of the SEY measurement method. Meanwhile, the SEY distribution adopted for multipactor threshold calculation is actually fitted from the experimental data of SEY with the SEY models,[14–17] and the resultant SEY discrepancy from the curve fitting further makes the prediction accuracy of multipactor threshold questionable. Hence, to properly evaluate the threshold result dispersion with respect to the SEY measurement error, a thorough analysis of multipactor threshold sensitivity to the material's SEY is highly needed in engineering practice.

With the purpose of multipactor prevention, the current research efforts in the study of multipactor are primarily contributed to exploring novel multipactor mechanisms,[18–21] and developing accurate predictive techniques[22–25] and efficient surface treatments for multipactor inhibition with inertial materials,[26,27] and micro-porous structures,[28–32] and diverse waveform.[33] On the contrary, there are a few studies concerned with the threshold sensitivity analysis where intensive threshold calculations are required. To the best of the authors' knowledge, the most relevant work on the threshold sensitivity is conducted for multipactor in a small-gapped[34] and parallel-plate[35] waveguide using particle-in-cell (PIC) simulations. However, this work only covers the first-order multipactor mode with the material of silver and also excludes the asymmetric multipactor case in coaxial lines, which is more commonly used in RF systems. In addition, the implementation of random secondary emission in PIC simulations leads to inevitable fluctuation in the threshold calculation result.[34] However, it can be eliminated by depicting the secondary emission randomness with the probability perspective in multipactor statistical modeling, which is of satisfactory accuracy and efficiency in the threshold calculation and, thus, more appropriate for the quantitative evaluation of multipactor threshold sensitivity. Presently, multipactor statistical modeling has been widely applied to multipactor in parallel plates (PMX) and coaxial lines (CMX) with either single-carrier or multi-carrier signal excitations,[36–38] as well as the single-surface multipactor on a dielectric surface.[39]

In this regard, this research is mainly dedicated to performing a comprehensive study of multipactor threshold sensitivity to the material's SEY property with statistical modeling, thus, providing useful guidance and reference for properly determining multipactor threshold margin from the SEY measurement error in practical engineering applications. In contrast to the prior literature, this study covers the threshold sensitivity analysis of both PMX and CMX with different frequencies and typical materials, where the significant effect of the device geometry, the multipactor mode, and the material type is included and the underlying mechanism for the sensitivity discrepancy between different SEY regions is explored for the first time. The main research content in this paper is organized as follows: First, the research methodology with the definition of SEY and the statistical modeling of two-surface multipactor is briefly introduced in Sec. II along with the parameter specification. Then, the threshold sensitivity quantification with the result and mechanism analysis is detailed in Sec. III. Finally, the conclusive summary is included in Sec. IV.

II. RESEARCH METHODOLOGY

In a general view, the threshold sensitivity in this study is evaluated by directly calculating the threshold variation corresponding to the specified SEY variation, and it is fulfilled according to the research flow charted in Fig. 1, which is similar to that of Ref. 34. First, requisite SEY curves are created by imposing additional SEY variation to the critical regions of the reference (average) SEY distribution; see more details of the SEY definition in Sec. II A. Then, multipactor threshold voltage of parallel plates and coaxial lines for the created SEY curves are calculated with the two-surface statistical modeling, which is introduced briefly in Sec. II B. Finally, the parameter specification of the involved device geometries, multipactor modes, and coating materials for the effect analysis is detailed in Sec. II C. On that basis, the quantification and the comparison of multipactor threshold sensitivity are conducted with the related mechanism analysis in Sec. III.

A. SEY definition

In light of the inherent correlation between multipactor formation and the SEY property, a typical SEY distribution is mainly characterized with the following SEY constants: the first and second crossover energies (E_1 and E_2), the SEY maximum (σ_m), and its corresponding energy (E_m). Taking them as the reference points, the whole SEY distribution can be roughly segmented to seven different regions of interest: R_1 (energies below E_1), R_2 (energies around E_1), R_3 (energies between E_1 and E_m), R_4 (energies around E_m), R_5 (energies between E_m and E_2), R_6 (energies around E_2), and R_7 (energies above E_2); see Fig. 2 for more details.

On this basis, the requisite SEY variation for evaluating the threshold sensitivity is introduced by tuning the SEY curve in each energy region. For practical implementation, the fitted SEY distribution from the result average of the SEY measurement at different impact energies is adopted as the reference SEY curve and denoted with C_R. Then, with an approach similar to Ref. 34, the tuned SEY curves are created by imposing gradual SEY variation with parabolic-like shape in each region according to the SEY dispersion caused by the SEY measurement error. Accordingly, these tuned SEY curves are denoted as C_T with additional superscripts of "+" and "−" adopted for differentiating the SEY increment and decrement relative to the reference SEY curve separately. It is worth mentioning that the energy regions of interest are tuned one by one with the other regions kept unchanged when evaluating the threshold sensitivity for the specified SEY region. To accurately reflect the SEY variation to the threshold variation, the above SEY curves are practically fed in the form of

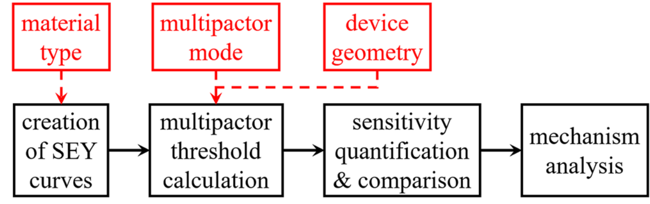

FIG. 1. Research flow for the quantitative analysis of multipactor threshold sensitivity.

Published under an exclusive license by AIP Publishing

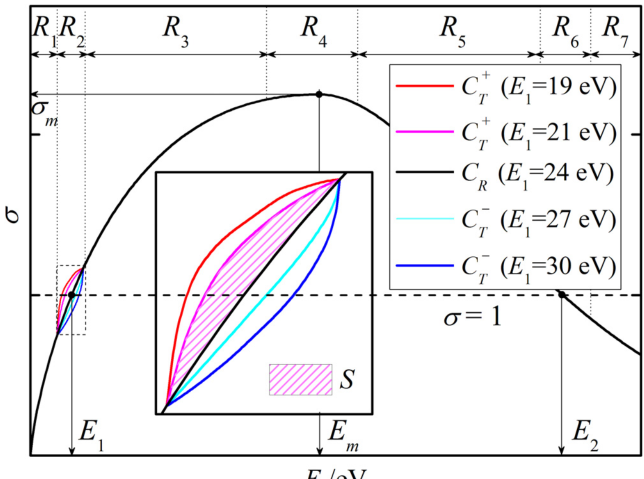

FIG. 2. Illustration of region segmentations for typical reference SEY curve C_R and tuned SEY curves C_T with respect to the value dispersion of E_1 around 24 eV. The inset window is a zoom-in of the tuned SEY curves in the dashed box for depicting the SEY variation within R_2, and the purple-shaded area refers to the total SEY variation S for the tuned curve with E_1 decreased to 21 eV. The condition of $\sigma = 1$ is marked out with the dashed line.

point-wise SEY data rather than the empirical formula of SEY to the statistical modeling detailed in Sec. II B.

For the sake of convenience, the primary object of this sensitivity analysis still adopts the technical Ag in Ref. 34, from which the created SEY curves are extracted and then reutilized in this study; see the main SEY constants in Table I. The SEY dispersion of Ag is as follows: $E_1 \in$ [19–24–30] eV, $E_m \in$ [200–250–450] eV, and $\sigma_m \in$ [2.06–2.17–2.30], which are collected from massive SEY measurements of the Ag samples. Taking R_2 for illustration, several tuned SEY curves are created by fitting E_1 to different values around the average of 24 eV, with almost uniform SEY variation and parabolic edges separately applied to the center and the boundary of the tuned SEY region. In the inset window of Fig. 2, the SEY increment relative to the reference SEY curve in R_2 is highlighted with the purple-shaded area for the tuned SEY curve with E_1 decreased to 21 eV. For quantitative analysis, the total SEY variation (denoted as S) in R_2 is evaluated with the following integral:

$$S(R_2) = \int_{R_2} (\sigma_T(E) - \sigma_R(E))dE, \tag{1}$$

where $\sigma_R(E)$ and $\sigma_T(E)$, respectively, represent the SEY value of the reference and tuned SEY curve at the specified impact energy E. Accordingly, the average SEY variation $\Delta\sigma$ can be quantified with

$$\Delta\sigma = S/\Delta E, \tag{2}$$

TABLE I. Main SEY constants of typical materials.

Material	σ_m	E_m/eV	E_1/eV	E_2/eV
Ag	2.17	250	24	3600
Au	1.79	1000	150	4000

where ΔE refers to the energy spread of the energy region under consideration. Comparatively, S which can take the region length into consideration is more appropriate for quantifying the SEY variation in the following sensitivity analysis.

B. Statistical modeling of two-surface multipactor

With the above-mentioned SEY definitions, the quantitative evaluation of multipactor threshold sensitivity still requires intense calculations of multipactor threshold for both the reference and tuned SEY curves. This study needs to perform the threshold analysis for both PMX and CMX with the general statistical modeling of two-surface multipactor,[37] which is also detailed here for completeness.

For either PMX or CMX, electron multiplication is contributed by the double-sided (DS) and single-sided (SS) impacts of secondary electrons on both surfaces, which are separately denoted as A and B in the following statistical formulation for differentiation. As illustrated in Fig. 3, they specifically refer to the bottom and top plate for PMX and likewise the inner and outer conductor for CMX. With that, two-surface multipactor statistical modeling is fulfilled by formulating the recurrent relation between the distribution functions over electron emission phase φ_s (the field phase at electron emission) in accordance with the electron interactions on both surfaces. The process formulation is performed on the same generation of electrons which are experiencing the same impacts. The population number and the emission phase distribution for the lth generation of electrons are denoted as N_l and $f_l(\varphi_s)$ separately, and the relevant parameters for the next generation of electrons are designated as N_{l+1} and $f_{l+1}(\varphi_s)$, respectively.

In view of the causal correlation between two adjacent generations of electrons illustrated in Fig. 3, the iterative solution of the above parameters on either surface can be expressed as

$$\begin{aligned} N_{l+1}^A f_{l+1}^A(\varphi_s) = N_l^A \int_0^{2\pi} K(\varphi_s - \varphi_s'|\varphi_s'; \xi_{AA}) f_l^A(\varphi_s') d\varphi_s' \\ + N_l^B \int_0^{2\pi} K(\varphi_s - \varphi_s'|\varphi_s'; \xi_{BA}) f_l^B(\varphi_s') d\varphi_s', \end{aligned} \tag{3}$$

and

$$\begin{aligned} N_{l+1}^B f_{l+1}^B(\varphi_s) = N_l^B \int_0^{2\pi} K(\varphi_s - \varphi_s'|\varphi_s'; \xi_{BB}) f_l^B(\varphi_s') d\varphi_s' \\ + N_l^A \int_0^{2\pi} K(\varphi_s - \varphi_s'|\varphi_s'; \xi_{AB}) f_l^A(\varphi_s') d\varphi_s'. \end{aligned} \tag{4}$$

Note that ξ refers to the electron trajectory with the specified emission (first subscript) and impact (second subscript) surfaces, and thus, the first and second integrals on the right hand account for the contributions from the SS and DS impacts, respectively.

When denoting the difference of electron emission phase $\varphi_s - \varphi_s$' as $\Delta\varphi_s$, the component function $K(\Delta\varphi_s|\varphi_s; \xi)$ can be further written, based on the periodic varying behavior of φ_s, as follows:

$$K(\Delta\varphi_s|\varphi_s; \xi) = \sum_{n=0}^{\infty} G(\Delta\varphi_s + 2n\pi|\varphi_s; \xi)\sigma(\Delta\varphi_s + 2n\pi|\varphi_s; \xi), \tag{5}$$

where $\sigma(\tau|\varphi_s; \xi)$ represents the SEY function for calculating the incident SEY, and it is actually interpolated from the point-wise SEY curves with the corresponding impact energy to the specified electron

Published under an exclusive license by AIP Publishing

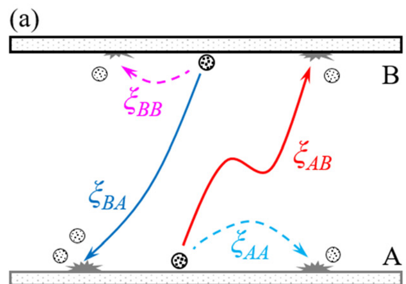

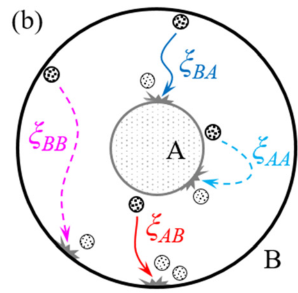

FIG. 3. Illustration of statistical modeling for two-surface multipactor established from double-sided (solid) and single-sided (dashed) impacts of secondary electrons on surface A and surface B, which, respectively, account for the bottom and top plates for the parallel-plate multipactor (a) and the inner and outer conductors for the coaxial multipactor (b).

trajectory ξ, which is of the deterministic transit time τ and emission phase φ_s; $G(\tau|\varphi_s;\xi)$ is the joint probability density function and physically represents the transition probability of electrons for the specified trajectory $\xi(\tau, \varphi_s)$. It is essentially built to transfer the randomness from velocity domain to time domain and thus determined with

$$G(\tau|\varphi_s;\xi) = \left|\frac{du(\tau|\varphi_s;\xi)}{d\tau}\right| f(u(\tau|\varphi_s;\xi)), \tag{6}$$

where $f(u)$ accounts for the probability density function of electron emission velocity u, and the right derivate term $u(\tau|\varphi_s;\xi)$ is a hypothetical function for correlating electron emission velocity with electron transit time. Specifically, $G(\tau|\varphi_s;\ \xi)$ can be solved with the analytical approach in Ref. 36 for PMX or the numerical approach in Ref. 23 for CMX separately.

On that basis, the effective SEY (σ_{eff}) for quantifying the temporal tendency of the electron population then can be determined with the following population ratio of two adjacent generations of electrons when the distribution of electron emission phase has evolved to stationary:

$$\sigma_{eff} = \frac{N_{st+1}}{N_{st}} = \frac{N^A_{st+1} + N^B_{st+1}}{N^A_{st} + N^B_{st}}. \tag{7}$$

Accordingly, multipactor threshold can be determined with the RF voltage for the condition $\sigma_{\rm eff} = 1$. On that basis, the relative variation of multipactor threshold voltage (denoted as δ) for the sensitivity evaluation can be further obtained with the following expression:

$$\delta = \frac{V^T_t - V^R_t}{V^R_t}, \tag{8}$$

where V_t^R and V_t^T account for the multipactor threshold voltage for the reference and tuned SEY curves, respectively.

C. Parameter specification for effect analysis

As mentioned above, this study is aimed at performing a comprehensive analysis of the threshold sensitivity with the effect of the device geometry, the multipactor mode, and the material type included. For this consideration, the material of Au in Ref. 40 is also included in the following sensitivity analysis in addition to the technical Ag; see their main SEY constants in Table I. Note that this study actually adopts clean Au with much lower SEY for the convenience of the following effect analysis, rather than the technical Au whose SEY is close to the technical Ag. In addition, the tuned SEY curves of Au are created similarly to Ag because of a lack of experimental SEY measurement data. As for the geometric parameters, the plate separation for PMX is set constant with $d = 1.0$ mm, while the CMX case adopts the typical 50Ω coaxial lines where the radii of the outer and inner conductors are set with $R_o = 3.55$ and $R_i = 1.54$ mm ($d = 2.01$ mm), respectively. Moreover, the sinusoidal electromagnetic field excited in the dominant TEM mode is assumed for both PMX and CMX, and the space charge effect is also neglected as in the previous research because our focus is still set on the multipactor onset condition in the threshold sensitivity analysis here.

Moreover, the following sensitivity analysis also covers multiple frequency points which correspond to different multipactor orders. For better illustration, the PMX and CMX susceptibility[36] zones of Ag are charted and plotted in Fig. 4 with the multipactor susceptibility curves of Au for comparison. It is worth to mention that CMX susceptibility zone changes with varying radius ratio; see more details in Ref. 41. The frequency points for the sensitivity analysis are specified with the product of fd equal to 1.2 GHz·mm (P_1), 10 GHz·mm (P_3), and 30 GHz·mm (P_4), which, respectively, correspond to the first-order, third-order, and higher-order PMX modes for the Ag material. Also, $fd = 3.0$ GHz·mm (P_2) is included here to cover the transition mode from the first-order to third-order PMX. However, the involved multipactor modes become different as a result of a shift of multipactor order in the CMX susceptibility zone. Whereas, for the material of Au, the frequency points of P_2 and P_3 are shifted to the first-order and third-order PMX modes separately due to the sharp shrinkage of multipactor zones with low SEY, which also results in multipactor not occurring for both P_1 and P_4 (CMX only).

III. SENSITIVITY QUANTIFICATION AND RESULT ANALYSIS

The above-mentioned research methodology provides the requisite basis for the quantitative analysis of the threshold sensitivity. The quantification approach of the threshold sensitivity with the comparative analysis of the sensitivity discrepancy between different regions and the underlying mechanism is detailed in this section.

A. Threshold result and sensitivity quantification

As prerequisite illustration of the sensitivity discrepancy between different SEY regions, Table II lists out the SEY variations [see Eqs. (1) and (2)] in each region and the corresponding relative variation of the

Published under an exclusive license by AIP Publishing

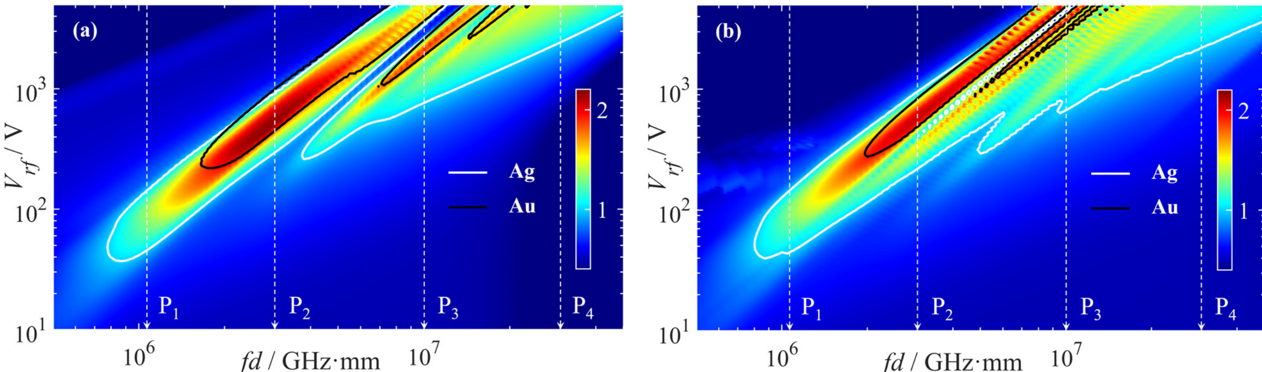

FIG. 4. Multipactor susceptibility chart of parallel plates (a) and 50Ω coaxial lines (b) for Ag (pseudo-color plot) with multipactor susceptibility curve of Ag (white) and Au (black). The quantitative analysis of multipactor threshold sensitivity is performed for the frequency points with the product of *fd* specified at 1.2 GHz·mm (P_1), 3.0 GHz·mm (P_2), 10 GHz·mm (P_3), and 30 GHz·mm (P_4). The gap *d* of the parallel plates is set constant at 1.0 mm, while the radii and the gap of the outer and inner conductor of the coaxial lines are set with $R_o = 3.55$, $R_i = 1.54$, and $d = 2.01$ mm, respectively.

PMX and CMX threshold voltage [see Eq. (8)] for the material of Ag. Note that only the data with most SEY increment are provided in Table II because practical research is more prone to avert the threshold over-estimate.

As shown in Table II, the result dispersion of the SEY measurement[34] ultimately leads to insignificant discrepancy between the magnitudes of $\Delta\sigma$ in different regions, which are roughly within the range of [0.09, 0.13] and slightly smaller in R_1 and R_2. The total SEY variation S is larger by two orders of magnitude in the regions with energies higher than E_1 for their relatively larger region length, especially for R_5 and R_7. However, there is little threshold variation in the statistical modeling results of both PMX and CMX even with considerable SEY variation in the regions of R_{4-7}, and this non-correlation can be found in the PMX threshold results of PIC simulations as well, where the relative error being lower than 1.1% is inevitable as explained in Ref. 34. Therefore, the following sensitivity analysis is mainly focused on the sensitivity comparison for the first three regions. Furthermore, the magnitude of δ in the statistical modeling results is roughly correlated with S for R_{1-3}, and both δ and S (magnitude) reach the maximum in R_3 following the PIC results. Regarding the discrepancy of $\Delta\sigma$ and S in different regions, it is more appropriate to evaluate and compare the threshold sensitivity of different regions with δ correlated with S. For that reason, the absolute slope of the δ–S curves is denoted as k and adopted for quantifying the threshold sensitivity. Additional superscripts and subscripts are adopted for all relevant parameters to differentiate the involved SEY regions and both cases of PMX and CMX, respectively. For instance, k_p^1 and k_c^2 separately refer to the threshold sensitivity of PMX at R_1 and CMX at R_2.

TABLE II. SEY variations in different regions and relative threshold variation of PMX and CMX with the material of Ag.

	Total and average SEY variation		PMX/CMX threshold variation
Region	$\Delta\sigma$	S/eV	$\lvert\delta\rvert$ /%
R_1	0.095	1.45	1.96/4.25
R_2	0.092	1.10	1.51/1.74
R_3	0.13	21.7	5.32/7.21
R_4	0.12	33.9	0
R_5	0.13	353.7	0
R_6	0.12	108	0
R_7	0.13	641.6	0

To illustrate the determination of k, the result of δ with response to gradual variation of S at different frequency points is calculated for both PMX and CMX with Ag as the material and plotted in Fig. 5. As can be seen, the y-axis range varies in different sub-figures, and the ratio of the y-axis range to the x-axis range in each sub-figure is set the same for the result plots of different regions, so that the threshold sensitivity can be intuitively evaluated and compared according to the curve slope. It shows that δ is generally with negative proportion to S for both PMX and CMX. Better linearity in the δ–S curves can be observed in most PMX results, but this linear trend can only be seen in the CMX results with low frequency (P_1 and P_2) from Figs. 5(a) and 5(b). The CMX results apparently become parabolic with positive concavity due to the nonlinear decrease in δ vs the increasing S, especially for the cases with negative magnitude of δ in Fig. 5(c). This is probably caused by the asymmetric distribution of electron impact energy on the inner and outer surfaces for the CMX formation. There are also discontinuous changes in the magnitude of δ with the variation of S for both PMX and CMX at high frequency points. As for the CMX result in the left part of Fig. 5(c), the magnitude of δ rises suddenly when S is almost decreased down to its minimum, where multipactor threshold is shifted upward to lower-order susceptibility boundary with the resultant shrinkage of the horned susceptibility zone as shown in Fig. 4. Likewise, more discontinuous variation of δ within the δ–S curves can also be observed in the PMX and CMX results of P_4 where more high-order multipactor zones are overlapped intensely. To address this problem, the value of k for the sensitivity comparison is mainly determined with linear curve fitting in the right-hand δ–S plot; see the dashed plots in Fig. 5(d).

Published under an exclusive license by AIP Publishing

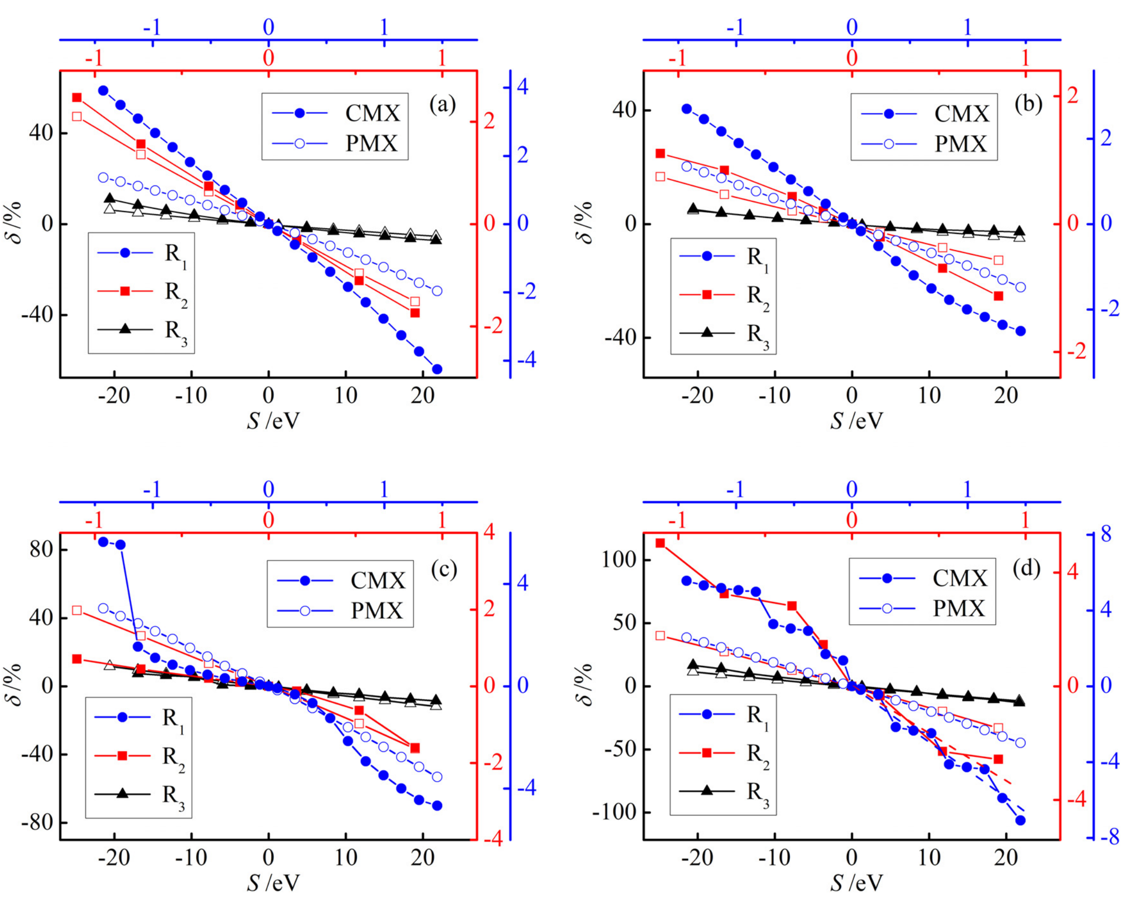

FIG. 5. Plots of the relative threshold variation of PMX (open) and CMX (solid) vs the total SEY variation in the regions of R_1 (blue circle), R_2 (red square), and R_3 (black triangle) for the frequency points of P_1 (a), P_2 (b), P_3 (c), and P_4 (d) specified in Fig. 4. The threshold sensitivity is quantified with the curve slope, which is determined with the linear fitting (dashed) for the nonlinear curve plot.

B. Effect analysis of multipactor threshold sensitivity

With the above-mentioned quantification approach of multipactor threshold sensitivity, the magnitude relation of multipactor threshold sensitivity between different regions is analyzed comparatively with the effect of the device geometry, the multipactor mode, and the material type included.

For the PMX result of P_1 shown in Fig. 5(a), the PMX threshold sensitivity of the first three regions is ordered as $k_p^2 > k_p^1 > k_p^3$ from the slope of the δ–S curves. Meanwhile, there shows magnitude increment of δ for all the regions when converted to the CMX case, and the increment of δ_c^1 is much larger than that of δ_c^2 (also see Table II for more details), which makes the order of the CMX threshold sensitivity converted to $k_c^1 > k_c^2 > k_c^3$. This indicates that the geometry conversion from the parallel plates to the 50Ω coaxial lines eventually makes the highest threshold sensitivity be transferred from R_2 to R_1 for the first-order multipactor. It is worth mentioning that there might be different sensitivity transfer for the geometry conversion to the CMX cases with other radius ratio (R_o/R_i). In addition to the order change, we are also able to find evident magnitude discrepancy between PMX and CMX sensitivity results at other frequency points from Fig. 5, which, thus, evinces the significant effect of the device geometry on multipactor threshold sensitivity.

Likewise, the related results in Figs. 5(b) and 5(c) also reveal significant magnitude variation in δ_p^2 of P_2 and δ_p^1 of P_3 with the frequency conversion, which, thus, alternates the order of PMX threshold sensitivity at these frequency points to $k_p^1 > k_p^2 > k_p^3$. However, the order of CMX threshold sensitivity remains $k_c^1 > k_c^2 > k_c^3$ for the frequency conversion results in a similar varying pattern of δ in each region. In most of the results, δ^3 is generally several times larger than δ^1 and δ^2, but more decrement in the magnitude of δ_c^3 than δ_c^1 in the P_2 result eventually leads to $\delta_c^1 \approx \delta_c^3$. For the convenience of sensitivity comparison, the sensitivity discrepancy can also be directly found from the plots in Fig. 6, where the PMX and CMX sensitivity results for different frequencies and materials are further summarized. For the result of P_4 in Fig. 5(d), more decrement of δ_p^1 compared to that of δ_p^2 also results in the magnitudes of k_p^1 and k_p^2 to be similar, while k_c^1 approaches k_c^2 with more increment of δ_c^2 compared to that of δ_c^1 as well. It indicates that the highest PMX threshold sensitivity is transferred back to R_2 with the frequency converted from P_3 to P_4 for both PMX and CMX. Meanwhile, we also find in Fig. 6(a) that CMX

Published under an exclusive license by AIP Publishing

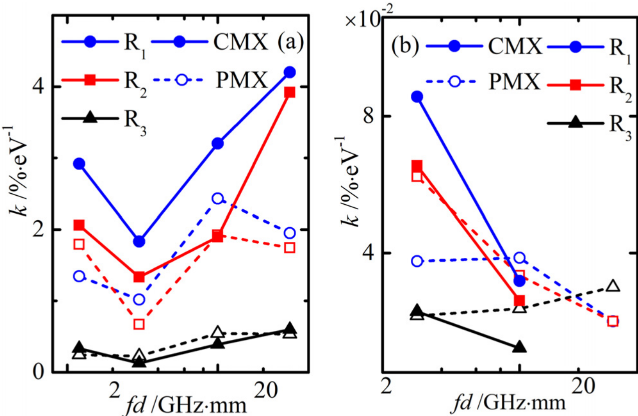

FIG. 6. Comparative plots of CMX (solid) and PMX (open) threshold sensitivity at the specified frequency points within the regions of R_1 (blue circle), R_2 (red rectangle), and R_3 (black triangle) for the materials of Ag (a) and Au (b). The other parameters are set the same as Fig. 4.

threshold sensitivity in the Ag result of all regions reaches its magnitude minimum at P_2, which can be explained with the densely distributed susceptibility curves nearby P_2 according to the plot of $\sigma_{\rm eff}$ in Ref. 36. Hereby, the above results inherently reveal the non-negligible dependence of the threshold sensitivity on the multipactor mode.

As for the effect of the material type, it can be found from Fig. 6(b) that the threshold sensitivity of Au is smaller than that of Ag by one to two orders of magnitude for both PMX and CMX, which is partially attributed to relatively larger region length of each SEY region for Au. However, there is still a much smaller (about one third in most results) magnitude of δ for Au compared to that of Ag, with response to the deterministic SEY variation. Meanwhile, the order of multipactor threshold sensitivity is also changed to $k_p^2 > k_p^1 > k_p^3$ for PMX in the Au result of P_2, which is different from the Ag result. However, for the Au result at P_4, the order of PMX threshold sensitivity also becomes $k_p^3 > k_p^1 \approx k_p^2$ with a sharp increase in k_p^3 and decrease in k_p^1 and k_p^2. In addition, the decreasing pattern of the CMX threshold sensitivity with the frequency conversion from P_2 to P_3 can also be found in the Au results for all regions, which is similar to the Ag result but with the conversion between different frequency points. Physically, the above significant variation of the threshold sensitivity with the material change is radically attributed to much lower SEY of Au. However, it is worth emphasizing again that the above sensitivity result with the clean Au cannot be directly applied to the technical Au, regarding the significant discrepancy of SEY between the clean and technical Au as mentioned above.

As revealed in the above results, multipactor threshold is most sensitive to the SEY variation in R_1 for most cases, which, however, is probably changed to R_2 and R_3 with a change in device geometry, multipactor mode, or coating material. In addition to comparing the threshold sensitivity between different regions, the δ–S curve plots in the above sensitivity result are also helpful for properly determining the threshold margin from the dispersion of SEY experimental measurements in practical applications. As indicated from the above Ag result, the magnitude of δ is greatly dependent on the involved effect and generally within the range of [2%, 13%] when $\Delta\sigma$ is specified around 0.1 in each SEY region. Meanwhile, there appears to be most threshold variation in R_3 owing to its relatively larger region length, but it is also possibly changed to R_2 at the transition mode between the first-order and third-order multipactor, where relatively smaller magnitude of k and δ can be found in all regions. Moreover, it is also able to find less threshold variation for the multipactor case with Au which is of lower SEY.

C. Mechanism analysis for the threshold sensitivity

To further investigate the underlying mechanism for the above sensitivity results, the impact energy distribution of electron impacts for threshold PMX and CMX at the specified frequency points is obtained with the statistical modeling in Sec. II and separately provided in Figs. 7 and 8 for the following comparative analysis. For better demonstration, the contributions by SS and all (DS+SS) impacts are both provided for comparative analysis.

As shown in Fig. 7, all of the distributions of electron impact energy for different cases are generally centered at the first crossover energy point which satisfies the threshold multipactor condition of $\sigma_{\rm eff} = 1$. Meanwhile, the regional coverage of electron impact energy is merely distributed to the first three regions, which is consistent with the non-correlation between multipactor threshold variation and the SEY variation in the regions of R_{4-7} as revealed in Table II. As for the result of P_1 in Fig. 7(a), a small proportion of SS impacts restricted in the left section of R_1 inherently reveals the predominant contribution

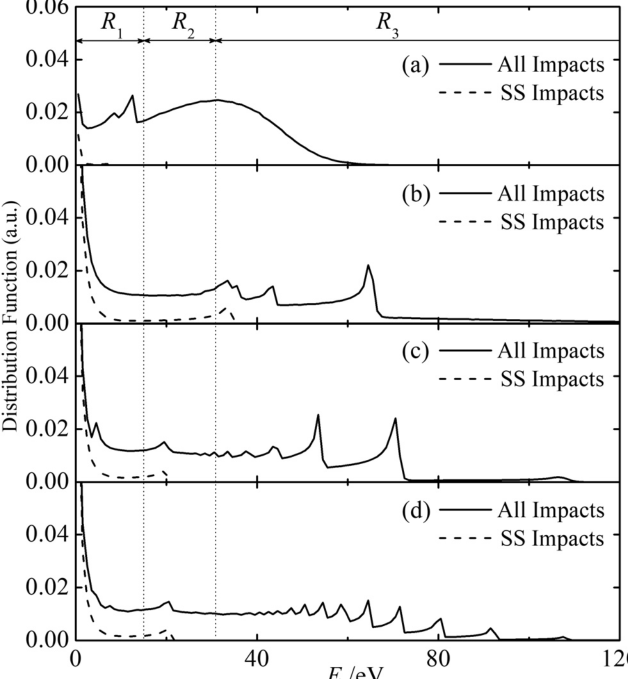

FIG. 7. Impact energy distribution of electron impacts (solid) for the threshold PMX case with the reference SEY curve of Ag at the specified frequency points of P_1 (a), P_2 (b), P_3 (c), and P_4 (d) in Fig. 4. The contribution by SS impacts is differentiated with the dashed line, and the coverage of electron impact energy in different SEY regions is delimited with the dotted lines for comparison.

Published under an exclusive license by AIP Publishing

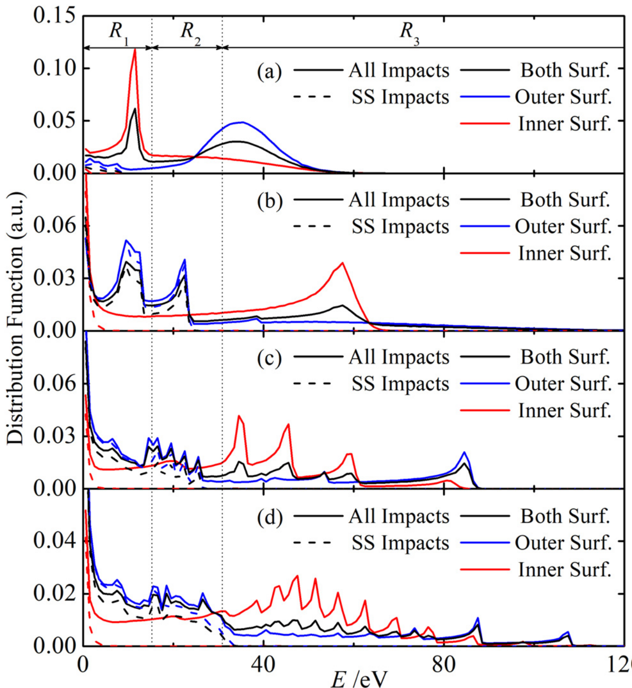

FIG. 8. Impact energy distribution of electron impacts (solid) on both surfaces (black), outer surface (blue), and inner surface (red) for the threshold CMX case with the reference SEY curve of Ag at the specified frequency points of P_1 (a), P_2 (b), P_3 (c), and P_4 (d) in Fig. 4. The contribution by SS impacts is differentiated with the dashed line, and the coverage of different regions is delimited with the dotted lines similar to Fig. 7.

of resonant DS impacts to the first-order PMX formation. It also shows that electron impact energy of all impacts is more concentrated around the intersecting boundary of R_2 and R_3. The density of electron impact energy within R_2 is higher than that of R_1, which conforms to relatively higher threshold sensitivity in R_2. However, there also shows largest proportion of electron impact energy within R_3, which is of lowest PMX threshold sensitivity oppositely. Note that this conflict is radically attributed to the partial coverage of electron impact energy within R_3, and thus, the total SEY variation in the right part of R_3 actually exerts negligible effect on the PMX threshold variation.

However, for the result of P_2 in Fig. 7(b), the frequency conversion ultimately leads to more SS impacts with the transition from the first-order to third-order PMX, and the enlarged distribution range of SS impacts correspondingly turns to cover both R_1 and R_2. Nevertheless, a significantly increased proportion of SS impacts within R_1 is still concentrated at its left section and accordingly inverts the order of PMX threshold sensitivity between R_1 and R_2, which can also be found in the results of P_3 and P_4. It is also apparently shown in Fig. 7(c) that the proportion of electron impact energy within R_1 and R_2 are partially transferred to R_3 with the frequency conversion from P_2 to P_3, which is in accordance with the increase in the PMX threshold sensitivity of R_3 shown in Fig. 6(a). Meanwhile, the coverage of electron impact energy within R_3 is expanded from its left part to the central region in the high-order PMX results. Especially for the result of P_4 in Fig. 7(d), further proportion decrement within R_1 eventually leads to a close density of electron impact energy in R_1 and R_2, which accords with the above sensitivity order of PMX threshold ($k_p^1 \approx k_p^2$) detailed in Fig. 6(a).

On the other hand, there also shows evidently different distribution of electron impact energy in the CMX results of Fig. 8 with the device geometry converted from parallel plates to coaxial lines. The impact energy distributions of electron impacts on the outer surface, the inner surface, and both surfaces are all provided in Fig. 8 regarding the asymmetry of CMX. As revealed from the result of P_1 in Fig. 8(a), the first-order CMX remains established mostly from DS impacts on both the outer and inner surfaces, while the SS impacts, with lesser contributions to the CMX formation, are still restricted to the left part of R_1. However, the impact energy distribution of DS impacts on the outer surface is markedly different from that of the inner surface due to the field non-uniformity in the coaxial lines. It shows that electron impact energy within R_2 is transferred to R_1 for DS impacts on the inner surface and simultaneously to R_3 for DS impacts on the outer surface, since the resultant ponder-motive force exerts an outward-pushing effect on the electron motions.[23] This transformation eventually forms a local spike near the center of R_1 in the impact energy distribution of DS impacts on the inner surface, and thus results in a larger density of electron impact energy within R_1 than that of R_2. This accordingly provides a good explanation for the order of the CMX threshold sensitivity ($k_c^1 > k_c^2$) as mentioned in Fig. 6(a). Furthermore, different distributions of electron impact energy on the outer and inner surfaces also indicate a potential discrepancy in the CMX threshold sensitivity on the SEY of different surfaces, which can also be found from the results of other frequency points in Fig. 8.

Meanwhile, we can also find significant variations in the impact energy distribution of the high-order CMX results in Fig. 8. When it transitions to high CMX order, the impact energy distributions within R_1 and R_2 turn out to be covered mostly by electron impacts on the outer surface, which probably comes from the contributions of long-term SS impacts with the above-mentioned outward-pushing effect. However, the impact energy distribution on the inner surface is still dominated by DS impacts similar to the PMX results, which accordingly keeps the order of the CMX threshold sensitivity as $k_c^1 > k_c^2$ in the results of P_2 and P_3. Moreover, the coverage expansion of electron impact energy in R_3 with the frequency conversion is also revealed in the CMX results of Fig. 8, and the transfer out of R_1 gradually makes the magnitude of k_c^1 approach to that of k_c^2 with the frequency converted to P_4, which is consistent with the sensitivity order of the CMX threshold ($k_c^1 \approx k_c^2$) detailed in Fig. 6(a).

Likewise, the effect of the material type on multipactor threshold sensitivity can also be revealed from different impact energy distributions of Au in Fig. 9, which shows obvious similarity to the Ag results. However, it can be seen from Fig. 9(a) that the impact energy distribution in the Au result of P_2 is similar to the Ag result of P_1, which is also consistent with the orders of the PMX sensitivity in Fig. 6(b). This is probably because a lower SEY distribution leads to a higher PMX threshold voltage, which actually corresponds to a lower multipactor order at the same frequency point according to the plot of multipactor zone and order in Ref. 36. Moreover, we can also find increasing coverage of electron impact energy within R_3 in Figs. 9(b) and 9(c) when converted to high frequency points, and it also eventually leads to the order of PMX threshold sensitivity ($k_p^3 > k_p^1 \approx k_p^2$) with full coverage of R_3 in the result of P_4. Meanwhile, we also find that the SEY variation close to E_m merely affects the threshold result with high multipactor order.

Published under an exclusive license by AIP Publishing

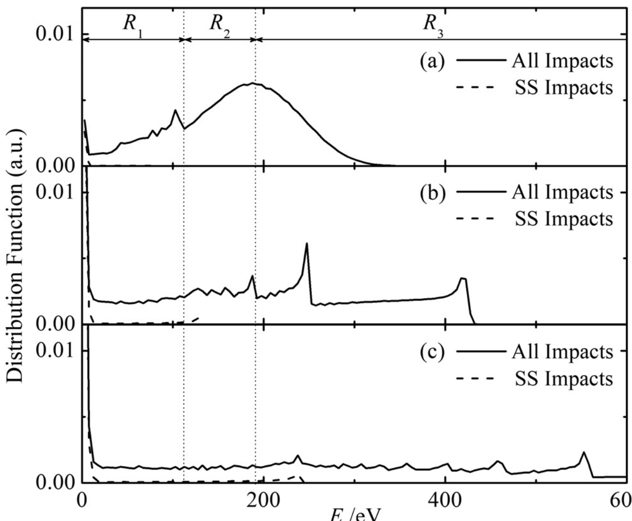

FIG. 9. Impact energy distribution of electron impacts (solid) for the threshold PMX case with the reference SEY curve of Au at the specified frequency points of P_2 (a), P_3 (b), and P_4 (c) in Fig. 4. The contribution by SS impacts is differentiated with the dashed line, and the coverage of different regions is delimited with the dotted lines similar to Fig. 7.

IV. CONCLUSIONS

In this paper, multipactor threshold sensitivity to the secondary emission yield (SEY) of microwave devices is quantitatively analyzed using the statistical modeling including the effect of the device geometry, the multipactor mode, and the material type, which has shown to be significant in this study but still disregarded in prior research of multipactor threshold sensitivity. Moreover, the underlying mechanism for the threshold sensitivity within critical energy regions is also thoroughly investigated based on the distribution of electron impact energy in these regions. The results indicate that the multipactor threshold sensitivity of both the parallel plates (PMX) and 50Ω coaxial lines (CMX) is mostly relevant to the energies below the energy corresponding to the SEY maximum (E_m). The threshold sensitivity discrepancy between different SEY regions is radically determined by the distribution of electron impact energy.

To be specific, multipactor threshold is most sensitive to the first energy region below the first crossover energy (E_1) for most cases, which further evinces the significance of accurate SEY measurement in the low-energy region. The highest threshold sensitivity can also be found within the energies around E_1 in the first-order PMX, which is dominated by the double-sided (DS) impacts on both surfaces. However, it eventually changed back to the first energy region with the geometry conversion to the first-order CMX, where DS impact on the inner surface is of primary contribution to asymmetric CMX formation but decelerated for the field non-uniformity. Meanwhile, it is also possibly changed to higher energies below E_m in the high-order multipactor with Au because of the gradual expansion of electron impact energy to E_m with a high threshold voltage or low SEY. It, thus, reveals non-negligible effect of the device geometry, the multipactor order, and the material type on the threshold sensitivity.

It also indicates that the SEY measurement error at the energies close to E_m merely affects the prediction accuracy of high-order multipactor threshold. Meanwhile, it is also able to find less threshold variation in the transition mode between the first and third multipactor order or multipactor cases with a low-SEY material. It can thus be concluded that the sensitivity analysis in this research can help to properly determine the threshold margin from the dispersion of SEY experimental measurement in practical engineering applications.

ACKNOWLEDGMENTS

This research was supported by the National Natural Science Foundation of China (Grant Nos. 61801370, U1537210, and 61971342), the Air Force of Scientific Research (AFOSR) MURI (Grant Nos. FA9550-18-1-0062 and FA9550-21-1-0367), and HPC Platform, Xi'an Jiaotong University.

AUTHOR DECLARATIONS

Conflict of Interest

The authors have no conflicts to disclose.

Author Contributions

Shu Lin: Formal analysis (equal); Funding acquisition (equal); Investigation (equal); Methodology (equal); Validation (equal); Visualization (equal); Writing – original draft (equal). **Hongguang Wang:** Funding acquisition (supporting); Validation (supporting); Writing – review & editing (supporting). **Hao Qu:** Formal analysis (equal); Investigation (equal); Validation (equal); Visualization (equal). **Ning Xia:** Formal analysis (equal); Investigation (equal); Validation (equal). **Patrick Wong:** Formal analysis (equal); Writing – review & editing (equal). **Peng Zhang:** Funding acquisition (supporting); Writing – review & editing (equal). **John P. Verboncoeur:** Funding acquisition (supporting); Writing – review & editing (supporting). **Meng Cao:** Funding acquisition (supporting); Writing – review & editing (supporting). **Yonggui Zhai:** Validation (supporting). **Yongdong Li:** Funding acquisition (supporting); Writing – review & editing (supporting).

DATA AVAILABILITY

The data that support the findings of this study are available from the corresponding author upon reasonable request.

REFERENCES

[1]J. R. M. Vaughan, IEEE Trans. Electron Devices **35**(7), 1172 (1988).
[2]C. Chang, J. Verboncoeur, M. N. Guo, M. Zhu, W. Song, S. Li, C. H. Chen, X. C. Bai, and J. L. Xie, Phys. Rev. E **90**(6), 063107 (2014).
[3]E. A. H. Sleiman, J. Hillairet, M. Belhaj, and S. Dadouch, Fusion Eng. Des. **185**, 113325 (2022).
[4]Z. Zhang, Y. Sun, W. Cui, H. Zhang, Y. Huang, and C. Chang, IEEE Trans. Electron Devices **66**(11), 4921 (2019).
[5]R. Udiljak, D. Anderson, P. Ingvarson, U. Jordan, U. Jostell, L. Lapierre, G. Li, M. Lisak, J. Puech, and J. Sombrin, IEEE Trans. Plasma Sci. **31**(3), 396 (2003).
[6]M. Mirmozafari, N. Behdad, and J. H. Booske, Rev. Sci. Instrum. **92**(8), 084706 (2021).
[7]S. V. Langellotti, N. M. Jordan, Y. Y. Lau, and R. M. Gilgenbach, Rev. Sci. Instrum. **92**(12), 124706 (2021).
[8]N. K. Vdovicheva, A. G. Sazontov, and V. E. Semenov, Radiophys. Quantum Electron. **47**(8), 580 (2004).

Published under an exclusive license by AIP Publishing

[9]M. Siddiqi and R. Kishek, Phys. Plasmas **26**(4), 043104 (2019).
[10]H. Yang, W. Huang, B. Zeng, and H. Wen, IEEE Trans. Electron Devices **68**(4), 1918 (2021).
[11]H. Ren and Y. Xie, Int. J. RF Microwave Comput. Aided Eng. **32**(3), e23002 (2021).
[12]X. Zhang, C. Chang, and B. Gimeno, IEEE Trans. Electron Devices **66**(11), 4943 (2019).
[13]N. Zhang, W. Cui, R. Wang, T. Hu, X. Wang, Y. Li, and S. Lin, in *Proceedings of the 8th International Workshop on Multipactor, Corona and Passive Intermodulation in Space RF Hardware* (ESA, Valencia, Spain, 2014).
[14]J. Sombrin, in *Proceedings of the Optique Hertzienne et Dielectriques (OHD)* (Sombrin TEEY Model, 1993).
[15]J. R. M. Vaughan, IEEE Trans. Electron Devices **36**(9), 1963–1967 (1989).
[16]M. Furman and M. T. F. Pivi, Phys. Rev. Spec. Top.-Accel. **5**(12), 124404 (2002).
[17]W. Cui, H. Zhang, Y. Li, Y. He, Q. Wang, H. Zhang, H. Wang, and J. Yang, Chin. Phys. B **27**(3), 038401 (2018).
[18]D. Wen, P. Zhang, J. Krek, Y. Fu, and J. P. Verboncoeur, Phys. Rev. Lett. **129**(4), 045001 (2022).
[19]X. Zhang, Q. Yu, and X. Ni, IEEE Trans. Electron Devices **69**(2), 748 (2022).
[20]Y. Zhai, H. Wang, L. Zhang, S. Lin, Y. Li, and Y. Li, IEEE Trans. Electron Devices **66**(12), 5333 (2019).
[21]A. Iqbal, P. Y. Wong, D. Wen, S. Lin, J. Verboncoeur, and P. Zhang, Phys. Rev. E **102**(4), 043201 (2020).
[22]L. Silvestre, Z. C. Shaw, T. Sugai, J. Stephens, J. J. Mankowski, J. Dickens, A. A. Neuber, and R. P. Joshi, J. Phys. D **55**(4), 045202 (2022).
[23]S. Lin, P. Sun, Y. Li, H. Wang, and C. Liu, Phys. Plasmas **27**(2), 022115 (2020).
[24]Y. Li, W. Cui, Y. He, X. Wang, T. Hu, and D. Wang, Phys. Plasmas **24**(2), 023505 (2017).
[25]W. Cai, T. Huang, C. Bai, Z. Zhao, X. Jin, B. Li, and Z. Yang, IEEE Trans. Electron Devices **69**(6), 3419 (2022).
[26]S. Mori, M. Yoshida, and D. Satoh, Phys. Rev. Accel. Beams **24**(2), 022001 (2021).
[27]V. Nistor, L. A. González, L. Aguilera, I. Montero, L. Galán, U. Wochner, and D. Raboso, Appl. Surf. Sci. **315**, 445 (2014).
[28]C. Chang, H. Huang, G. Liu, C. Chen, Q. Hou, J. Fang, X. Zhu, and Y. Zhang, J. Appl. Phys. **105**(12), 123305 (2009).
[29]M. Ye, Y. Li, Y. He, and M. Daneshmand, Phys. Plasmas **24**(5), 052109 (2017).
[30]X. Qiu, M. A. Saed, J. J. Mankowski, J. Dickens, and R. P. Joshi, AIP Adv. **11**(2), 025039 (2021).
[31]C. Chang, Y. Li, J. Verboncoeur, Y. Liu, and C. Liu, Phys. Plasmas **24**(4), 040702 (2017).
[32]C. Chang, Y. Liu, J. Verboncoeur, C. Chen, L. Guo, S. Li, and X. Wu, Appl. Phys. Lett. **106**(1), 014102 (2015).
[33]D.-Q. Wen, A. Iqbal, P. Zhang, and J. P. Verboncoeur, Appl. Phys. Lett. **121**(16), 164103 (2022).
[34]N. Fil, M. Belhaj, J. Hillairet, and J. Puech, Phys. Plasmas **23**(12), 123118 (2016).
[35]N. Fil, M. Belhaj, J. Hillairet, and J. Puech, in presented at the Microwave Symposium (IMS), in Proceedings of the IEEE International Microwave Symposium, 2016.
[36]S. Anza, C. Vicente, J. Gil, V. E. Boria, B. Gimeno, and D. Raboso, Phys. Plasmas **17**(6), 062110 (2010).
[37]S. Lin, H. Wang, Y. Li, C. Liu, N. Zhang, W. Cui, and A. Neuber, Phys. Plasmas **22**(8), 082114 (2015).
[38]S. Anza, M. Mattes, C. Vicente, J. Gil, D. Raboso, V. E. Boria, and B. Gimeno, Phys. Plasmas **18**(3), 032105 (2011).
[39]A. G. Sazontov and V. E. Nevchaev, Phys. Plasmas **17**(3), 033509 (2010).
[40]ECSS Secretariat, "Space engineering: Multipaction design and test" Technical Report No. ECSS-E-20-01A (ESA-ESTEC Requirements and Standards Division, ESA-ESTEC, Noordwijk, The Netherlands, 2013).
[41]S. Lin, N. Xia, H. Wang, Y. Li, and C. Liu, Acta Phys. Sin. **67**(22), 227901 (2018).

Published under an exclusive license by AIP Publishing